

Brisan, C., Ioan, R., Munteanu, L., Dumitriu, D. and Rugina, C., 2016. A natural sonic composite – the atmosphere. *Romanian Journal of Technical Sciences - Applied Mechanics*, 61(2), pp.125-143.

A NATURAL SONIC COMPOSITE – THE ATMOSPHERE

CORNEL BRISAN¹, RODICA IOAN^{2,3}, LIGIA MUNTEANU³,
DAN DUMITRIU³, CRISTIAN RUGINA³

Abstract. The atmosphere represents a natural sonic composite exhibiting the full band-gaps and localized modes around inhomogeneities given by the wind-velocity jumps. The paper analyses a barometric model including inhomogeneities which are modelled as Somigliana dislocations. The motion of atmospheric air is characterised by anharmonic coupling of nonlinear baroclinic fields of waves, and it is possible to tend to chaos when subjected to severe acoustic pulses. The riddling bifurcation is depicted that explains the generation of the hyperchaotic attractors.

Keywords: atmospheric models, Eshelby theory, full band-gap, hyperchaotic attractor, Riddling bifurcation.

1. INTRODUCTION

The sonic structures exhibit localized modes around interfaces or inhomogeneities due to the lack of purely real wave vector for certain frequencies, sustaining the evanescent modes [1]. The generation of evanescent modes are related to the existence of band-gaps or Bragg reflections at different frequencies inverse proportional to a specific internal distance [2–9]. If the band-gaps are not wide enough, their frequency ranges do not overlap. Consequently, any wave is reflected completely from layered structure in the frequency range where all the band-gaps for the different periodical directions overlap.

In this article we will discuss the existence in nature of structures that exhibit characteristics of sonic structures. It is the case of the atmosphere.

Simple models of the atmosphere are known starting to 1947's [10–13]. The frictionless laminar adiabatic motion of a rotating baroclinic fluid was discussed by Eady [10] in connection to cyclone waves and long waves of middle and high latitudes. During the 1950's, Lorenz examined the extend of which the linear statistical models are appropriate to be used in meteorology and the weather forecasting.

¹ Technical University of Cluj-Napoca, Romania

² Spiru Haret University, Bucharest, Romania

³ Institute of Solid Mechanics of the Romanian Academy, Bucharest

Description of the butterfly effect was presented in 1969 [14]. In the years that followed, a large number of papers analyze and emphasize the dynamic instability of the atmosphere [15].

The stability of a simple two-layer model of the baroclinic atmosphere was demonstrated by Brojewski [16].

The solitary waves with constant travelling speeds and the lack of dispersion are the key for stability. Some basic factors which can influence the atmospheric stability like the vertical variability of the wind are investigated by Brojewski [17, 18] and Tsuchida [19] with emphases to oscillation character after Hopf bifurcations of the second kind. The large-scale weather phenomena are sometimes associated to vortices originated from dynamical disturbances in the atmosphere.

The aim of this paper is to show that the atmosphere exhibits the full band-gaps and localized modes around inhomogeneities. Inhomogeneities due to stratified wind-velocity are modelled as Somigliana dislocations according to the Eshelby theory [20–22] and Wang *et al.* [23]. If the applied stress is σ_{wind} and the displacement field of stratified wind-velocity is v_{wind} , the force is given by

$$F_{wind} = \oint_{\Sigma} (v_{wind} \nabla \sigma_{wind} - \sigma_{ind} \nabla v_{wind}) ds, \quad (1)$$

where Σ is the closed surface which encloses the wind-velocity jumps [24] when point sources of explosive character act upon the atmosphere, riddling bifurcation can occur. In this bifurcation, one of the unstable periodic orbit embedded in a higher-dimensional chaotic attractor becomes unstable transversely to the attractor [25–29]. The hyperchaoticity can be related to Sommerfeld effect which is a universal phenomenon which is a result of the law of energy conservation [6, 24, 30, 33–35].

2. THE MODEL OF ATMOSPHERE

Two-layer model of baroclinic atmosphere referred to as a β -plane (Fig.1) is considered [16]. The isobaric levels are p_i , $i = 1, 2, 3, 4$.

The equations of the model are

$$\nabla^2 \zeta_t^{(3)} + J(\zeta^{(3)}, \nabla^2 \zeta_t^{(3)} + f) = f \frac{\omega^{(2)}}{\Delta p}, \quad (2)$$

$$\nabla^2 \zeta_t^{(1)} + J(\zeta^{(1)}, \nabla^2 \zeta_t^{(1)} + f) = -f \frac{\omega^{(2)}}{\Delta p}, \quad (3)$$

$$(\zeta_{,t}^{(3)} - \zeta_{,t}^{(1)}) + J \left(\frac{1}{2} (\zeta^{(1)} + \zeta^{(3)}), \zeta^{(3)} - \zeta^{(1)} \right) + \frac{g\sigma}{f} \omega^{(2)} = 0, \quad (4)$$

where $\zeta^{(1)}, \zeta^{(3)}$ are vorticity at the levels 1 and 3, $f = 2\Omega \sin \phi$ is the Coriolis parameter, Ω the angular velocity of the Earth, and ϕ the latitude, $\beta = \frac{df}{dz} = \text{const.}$,

$\omega^{(2)} = \frac{dp}{dt}$ is the vertical velocity at the level 2 in the pressure system, $u^{(i)}$ ($i=1,3$) the main air flow velocity at the levels 1 and 3, σ is the stability coefficient of the atmosphere, g the acceleration of gravity.

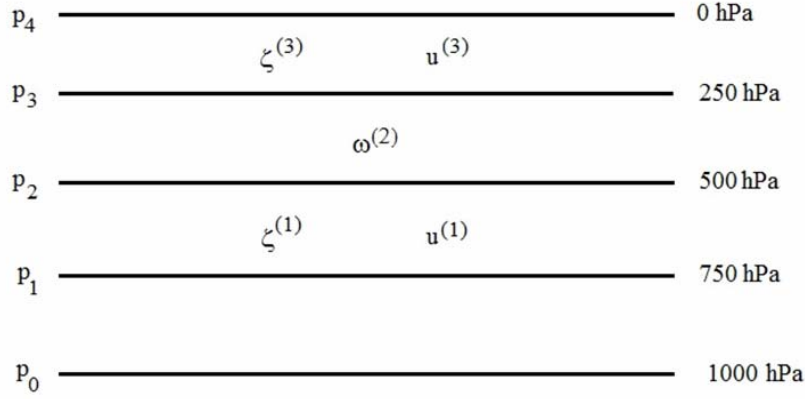


Fig. 1 – Structure of the atmosphere in the baroclinic model.

Let us consider the case when a turbulent region is surrounding the wind-velocity jumps. The applied stress σ_{wind} and the displacement field of stratified wind-velocity v_{wind} are related by the force expressed in (1), where Σ is the boundary of a volume $V_t \subset V$ where the wind-velocity jumps are present. V is a finite domain where the motion is studied.

Suppose that a constant vorticity field is prescribed into $V_t \subset V$

$$\zeta^{(j)}(y, z) = \begin{cases} \zeta^{(j)*}, & (y, z) \in V_t, \quad j = 1, 3 \\ 0, & (y, z) \in V/V \end{cases}. \quad (5)$$

Attention is paid to the boundary conditions attached to (2)–(5). The boundary conditions are imposed in terms of the displacement discontinuities, in accordance with the Somigliana dislocation. In addition, the normal component of

the velocity vanishes at the surface of the earth, the momentum vanishes at the limit of the atmosphere. The discontinuities are tangential and differ only by the wind velocity which is locally planar. The wind plan D is denoted by $(y^{\text{obs}}, z^{\text{obs}})$.

The coordinates y, z represent the east and north directions, respectively. The reference frame (y, z) is obtained by a Galilean transformation and moves with a constant velocity $v_{\text{wind}} = \frac{1}{2}(v^{+\text{obs}} + v^{-\text{obs}})$, where $v^{+\text{obs}}$ and $v^{-\text{obs}}$ are velocities on the left and right sides of D . The relative velocity is defined as $v_r = v^{-\text{obs}} - v^{+\text{obs}}$. Some symmetries are depicted $v^- = -v^+ = v_r/2$. Fig. 2a presents the bulk velocity on the left (+) and right (-) on the transition in the frame $(y^{\text{obs}}, z^{\text{obs}})$ and the same configuration after a Galilean transformation to the (y, z) frame moving with velocity V is displayed in Fig. 2b.

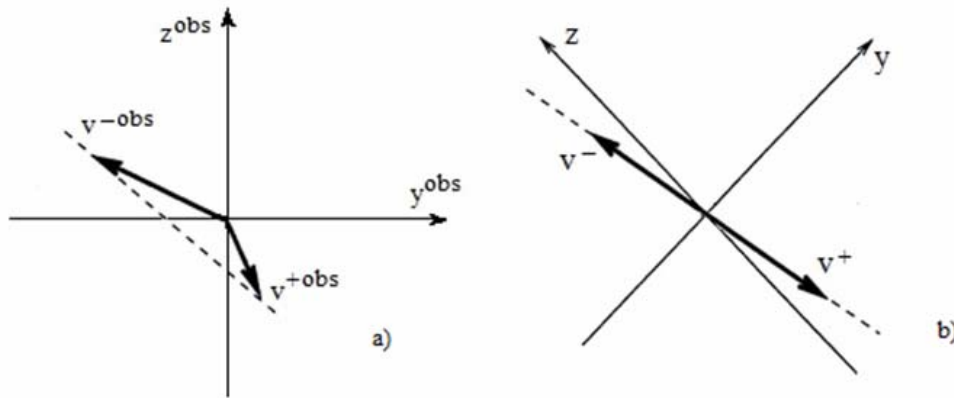


Fig. 2 – The bulk velocity on the left (+) and right (-) on the transition in the frame $(y^{\text{obs}}, z^{\text{obs}})$ (a) and the same configuration after a Galilean transformation to the (y, z) frame moving with velocity v_{wind} (b).

The weather forecast the equivalent barotropic atmosphere can be of interest of this paper [13]. The large scale perturbations in the atmosphere have the character of external waves in which the streamlines or isobars is approximately the same at all levels. Also, the increase of wind with height is similar along all verticals. So, the vorticity equation is given by

$$(f + \zeta)_t + f \rho^{-1} [(\rho U)_{,x} + (\rho V)_{,y}] = 0, \quad (6)$$

where ζ is the vertical vorticity component relative to the earth, are the components of velocity in the y (east), z (north) directions, ρ is the density. By

averaging (6) in the vertical direction with respect to pressure, and using the subscript “0” to denote the surface values, we have

$$\overline{(f + \zeta)}_{,t} = f p_0^{-1} p_{0,t} - f H^{-1} w_0, \quad (7)$$

where $H = RT_0 g^{-1}$ is the height of the homogeneous atmosphere, w is the vertical velocity component, p is the pressure, T the temperature and R the specific gas constant.

The velocity field is function on y, z, p, t . Let us supposed to have

$$U = \bar{u}(y, z, t)A(p), \quad V = \bar{v}(y, z, t)A(p), \quad (8)$$

that means $A(\bar{p}) = 1$ at a certain level \bar{p} . In this case $\bar{u} = U, \bar{v} = V$ and $\zeta = \bar{\zeta}$.

The equivalent barotropic level equation is obtained from (7) at the level $p = \bar{p}$

$$\zeta_{,t} + \left(U \frac{\partial}{\partial x} + V \frac{\partial}{\partial y} \right) (f + \bar{A}^2 \zeta) = f p_0^{-1} p_{0,t} - f H^{-1} w_0. \quad (9)$$

The equation (9) describes the motion of the barotropic atmosphere at the equivalent barotropic level $p = \bar{p}$. After eliminating the horizontal divergence by means of the continuity equation, we can introduce the geostrophic vorticity ζ_g at the equivalent barotropic level into (9)

$$\zeta_{g,t} + \bar{A}^2 (u_g \zeta_{g,x} + v_g \zeta_{g,y}) + \beta v_g = f p_0^{-1} p_{0,t} - f H^{-1} w_0, \quad (10)$$

where u_g, v_g are the components of the geostrophic wind, $\beta = f_{,y}$.

In the following the pressure can be replaced by the height Z of the isobaric surface

$$u_g = -g f^{-1} Z_{,z}, \quad v_g = g f^{-1} Z_{,y}. \quad (11)$$

Also, we have

$$\zeta_g = g f^{-1} (Z_{,zz} + z_{,yy}), \quad p_{,t} = g \rho Z_{,t}. \quad (12)$$

The frictional damping becomes important after a certain amount of time to explain the stationary perturbations. The component of velocity u_g verifies the motion equation with friction

$$u_{g,t} = f v_g = -F u_g, \quad (13)$$

where

$$F = \frac{\sin 2\alpha \sqrt{Kf}}{\sqrt{2} H}, \quad (14)$$

with α the angle between the isobars and the surface wind and K the eddy diffusivity.

By introducing (11–14) into (10) we obtain an equation in $Z(y, t)$. By a variable change $\eta = k_y y + k_z z - \omega t$, for the solutions $\zeta^{(1)}$ and $\zeta^{(3)}$ of (2)–(5), and the solution ζ of the equation in Z , can be taken under the form by applying the cnoidal method [37]

$$\theta_l(\eta) = \sum_{j=1}^n \alpha_{jl} \text{cn}^2[\eta_{jl}; m_{jl}] + \frac{\sum_{j=0}^n \beta_{jl} \text{cn}^2[\eta_{jl}; m_{jl}]}{1 + \sum_{j=0}^n \gamma_{jl} \text{cn}^2[\eta_{jl}; m_{jl}]}, \quad l = 1, 2, 3, \quad (15)$$

where $0 \leq m_{jl} \leq 1$, $l = 1, 2, 3$, $j = 1, 2, \dots, n$. By introducing (15) into (2)–(4) and equation in Z , the unknowns α_{jl} , β_{jl} and γ_{jl} are determined by using a genetic algorithm.

The recurrent equations for higher order terms of the dispersion function $\mu(\mu_l)$ are given by

$$\mu_{s, \eta \eta} + \left[K_s^2 + K_s + F_{sm}(\alpha_{jl}, \beta_{jl}, \gamma_{jl}, m_{jl}) \right] \mu_m - \Omega_s(\alpha_{jl}, \beta_{jl}, \gamma_{jl}, m_{jl}) = 0, \quad (16)$$

$$l = 1, 2, 3, \quad j = 1, 2, \dots, n, \quad s = 1, 2, 3, \dots$$

where the constants K_s , $s = 1, 2, \dots$ and the functions $F_s(\alpha_{jl}, \beta_{jl}, \gamma_{jl}, m_{jl})$, $m = 1, 2, \dots$, are known numerically.

3. ANALYSIS

The simulation is carried out for isobaric levels of 1 000, 750, 500, 250 and 0 hPa, $\sigma = 0.8R\sigma_0/g$, $\sigma_0 = -50\text{K}/1000 \text{ hPa}$, $\beta = 1.5 \times 10^{-11} \text{m}^{-1} \text{s}^{-1}$, $\alpha^2 = 1.5 \times 10^{-12} \text{m}^{-2}$ and $\Delta p = 500 \text{hPa}$. First functions $F_s(\alpha_{jl}, \beta_{jl}, \gamma_{jl}, m_{jl})$, $m = 1, 2, 3, 4$, are represented in Fig. 3. The calculus shows that functions $F_s \leq 0.4$ for all m .

First functions $\Omega_s(\alpha_{jl}, \beta_{jl}, \gamma_{jl}, m_{jl})$, $m = 1, 2, 3, 4$, are represented in Fig.4. Similarly, these functions verify the condition $\Omega_s \leq 1.2$ for all m . First four constants K_s , $s = 1, 2, 3, 4$, are 8.2540; -4.2388 ; 0.4111 and 2.3433. The variation of the real and imaginary parts of the dimensionless solution with respect to dimensionless solutions $\zeta^{(1)}/\zeta_{10}$ and $\zeta^{(3)}/\zeta_{30}$ are presented in Fig.5. The particular solutions $z_0, \zeta_{10}, \zeta_{30}$ correspond to linear case when the Jacobians become zero. The red and orange colors correspond to linear case when the solutions are known as modon and Rossby's waves.

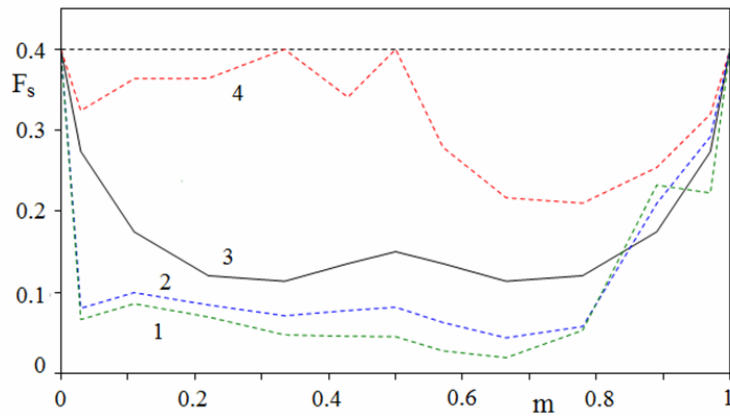


Fig. 3 – First four functions $F_s(\alpha_{jl}, \beta_{jl}, \gamma_{jl}, m_{jl})$, $s = 1, 2, 3, 4$.

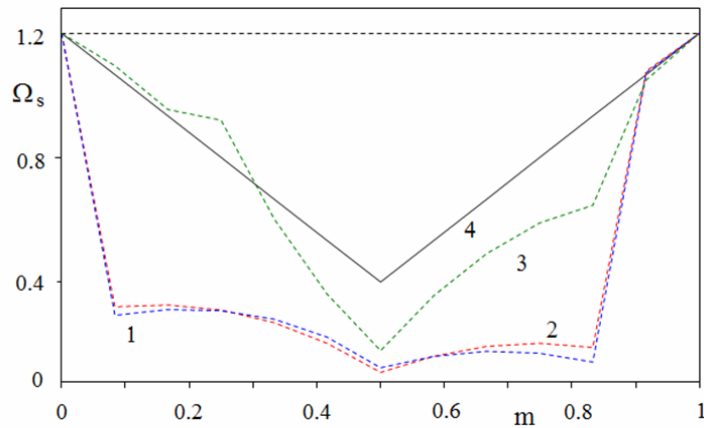


Fig. 4 – First four functions $\Omega_s(\alpha_{jl}, \beta_{jl}, \gamma_{jl}, m_{jl})$, $s = 1, 2, 3, 4$.

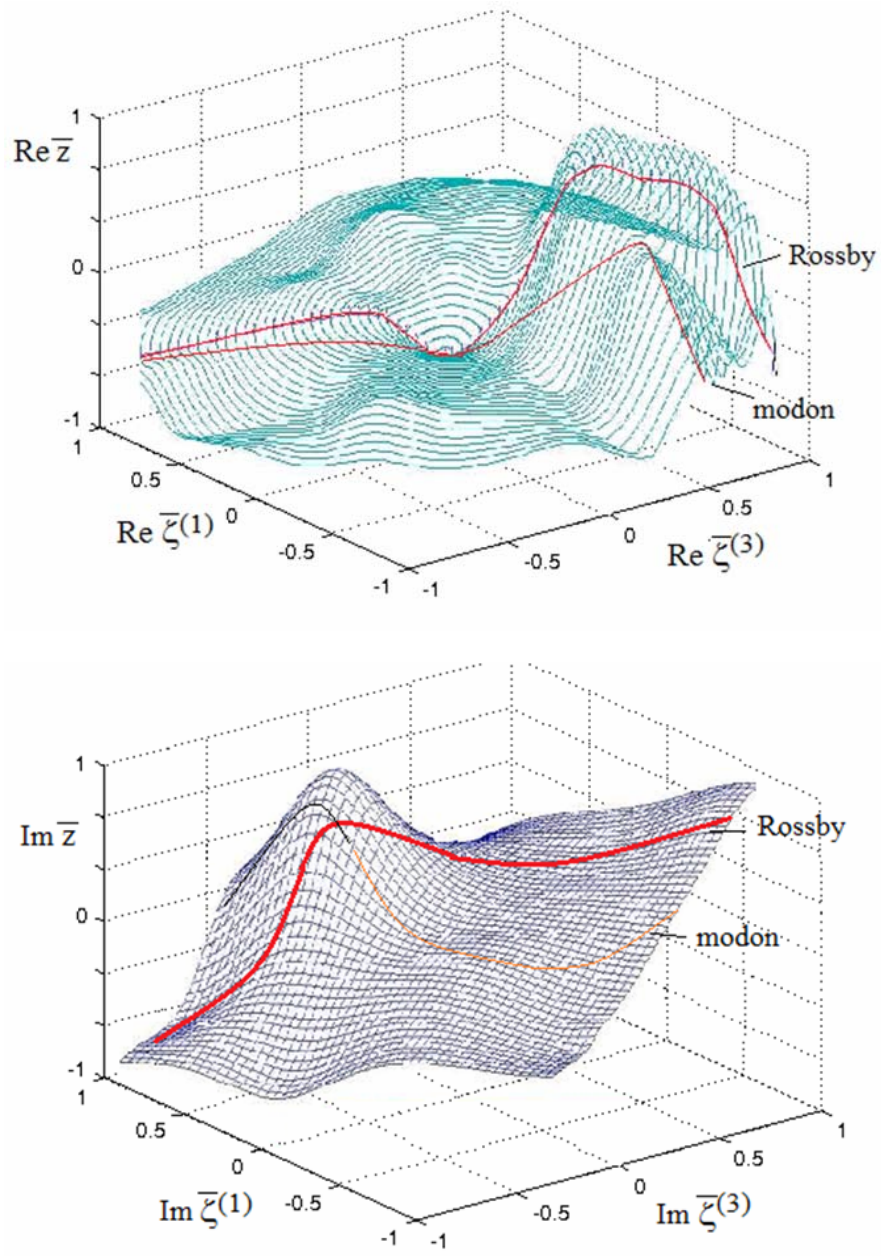


Fig. 5 — Variation of the real part (up) and the imaginary part (down) of the dimensionless solution \bar{z} with respect to dimensionless solutions $\bar{\zeta}^{(1)}$ and $\bar{\zeta}^{(3)}$.

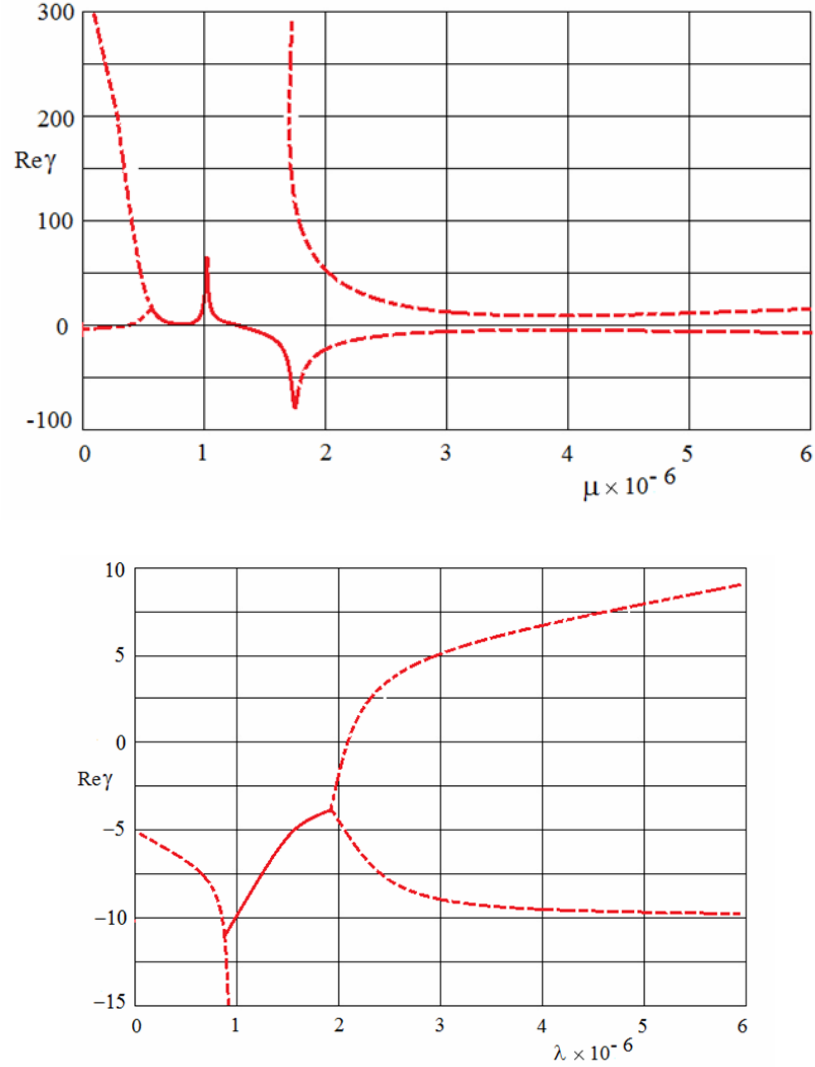


Fig. 6 – Dispersive curve for modon (up) and Rossby waves (down).

The linear case is obtained for vanishing of the Jacobians in (2)–(5), i.e. $\nabla^2\psi = \mu^2\psi$ and $\nabla^2\psi = -\lambda^2\psi$. Figure 6 displays the dispersion curves for modon (up) and Rossby's waves (down) for $\gamma = c - \bar{u}$, $c = \frac{\omega}{k}$, $\bar{u} = 10$ m/s. Similar results are reported by Brojewski [16].

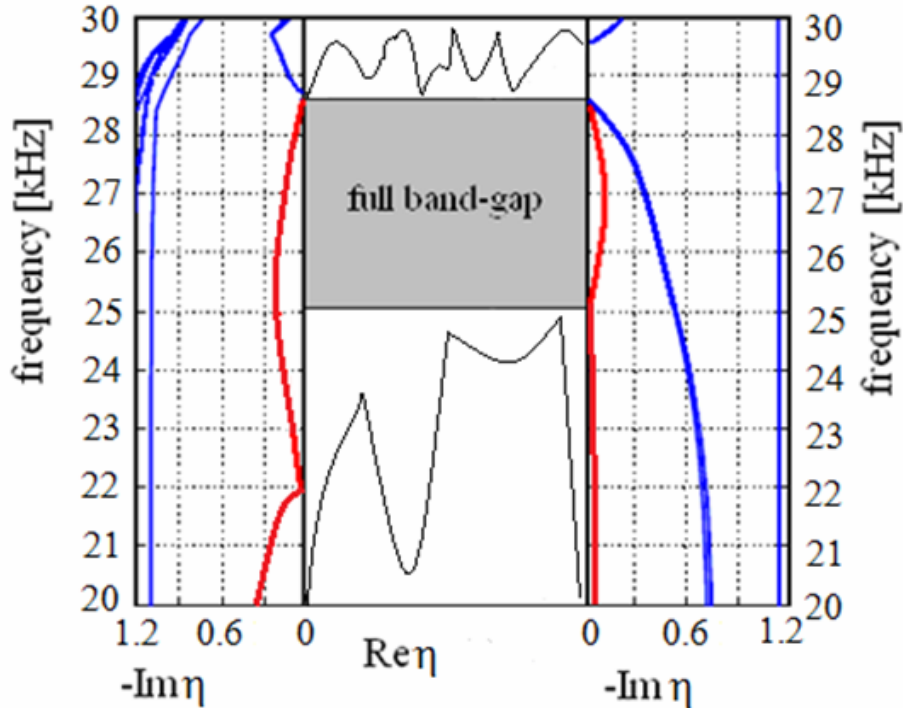


Fig. 7 – Band structure for the atmosphere.

The atmosphere with stratified wind-velocity has the properties of a sonic structure. The guided waves are accompanied by evanescent waves. Using the Joannopoulos representation [8] for the band-gap structure, Fig. 7 presents the band structure of the atmosphere model. The central grey region is the full band-gap ranged between 25 kHz and 28.5 kHz, given by the real part of the wave vector. The left region represents the imaginary part of the wave vector for y (east) direction, while the right region is the imaginary part of the wave vector for z (north) direction. The red lines represent the imaginary part of the wave vector of the evanescent modes inside the band-gap.

If need to have a full band-gap, the band-gaps for both east and north directions must be in the same frequency region. The stratified wind-velocities cause narrow partial gaps at different frequencies which do not overlap. As mechanical contrast increases, the partial gaps widen and begin to overlap in the same frequency region leading to a full band-gap independent of the polarization.

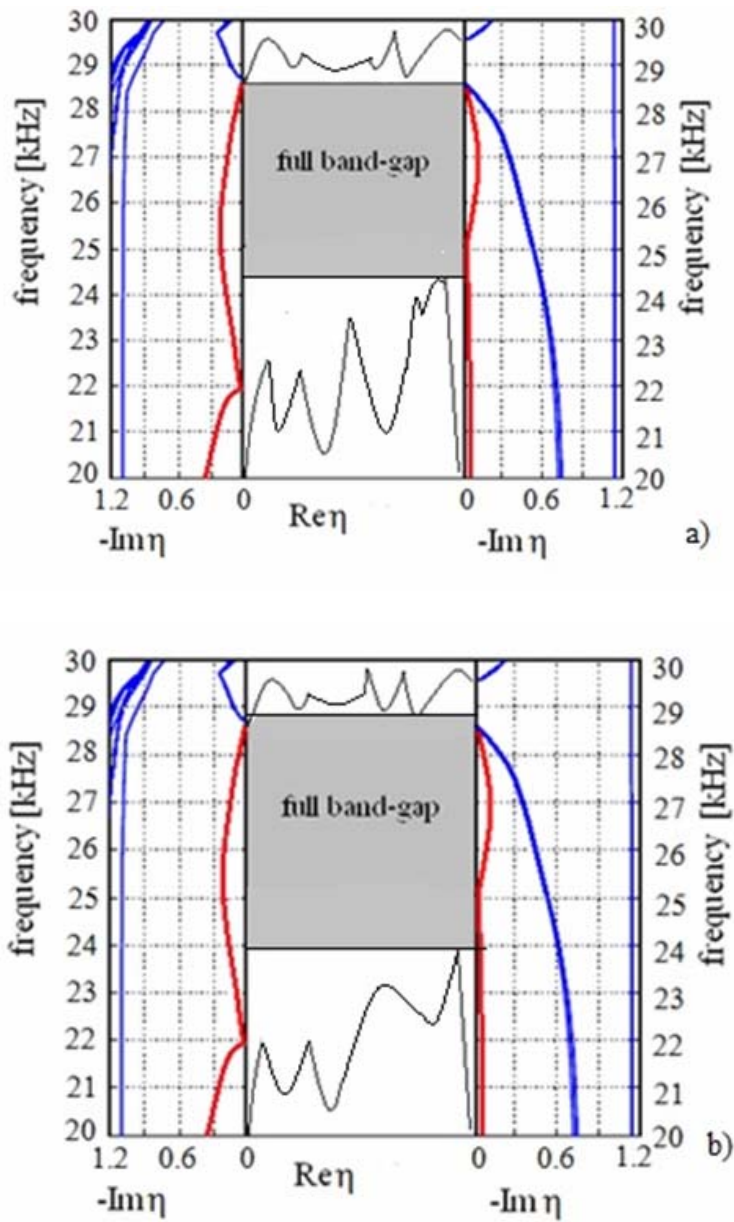


Fig. 8 – Band structure for the atmosphere for (a) Gaussian source incidence, and (b) point source incidence.

The atmosphere subjected to acoustic pulses of explosive character (surface explosion or volcano) coming from point source or Gaussian beam, has

surprisingly more pronounced properties of a sonic structure. Figure 8 presents the band structure of the atmosphere in this case, for (a) Gaussian source incidence, and (b) point source incidence. It can be seen a significant increase of the full band-gap in both loading cases.

In what concerns the incident sources, we calculate the pressure field for point source and Gaussian source incidence, at frequency of 27 kHz inside the full band-gap.

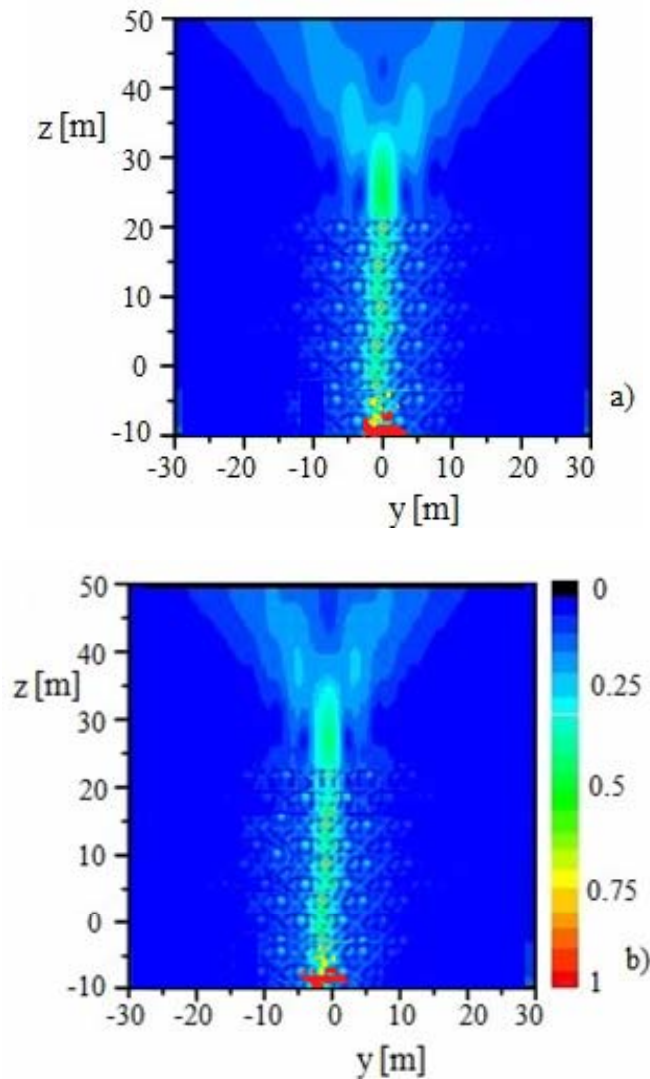


Fig. 9 – Imaging pressure field for (a) Gaussian source incidence, and (b) point source incidence.

From Fig. 9 we see that the pressure field is independent to the incident source for both the Gaussian and point incident sources. This fact is interesting because by tuning the length of the waveguide, the distance between source and image can be easily controlled.

4. CHAOS AND HYPERCHAOS

If the model (2)–(5) is subjected to acoustic pulses of sufficient amplitude $0.5 \leq a/a_0 \leq 1$, where a_0 is a reference value, the motion becomes chaotically. A complex pattern is given by the motion of disordered waves $\bar{\zeta}^{(1)}$ and $\bar{\zeta}^{(3)}$ aggregated into large amplitudes. Fig. 10 shows the flow of the disordered waves for (a) Gaussian source incidence, and (b) point source incidence, for $a/a_0 = 0.75$.

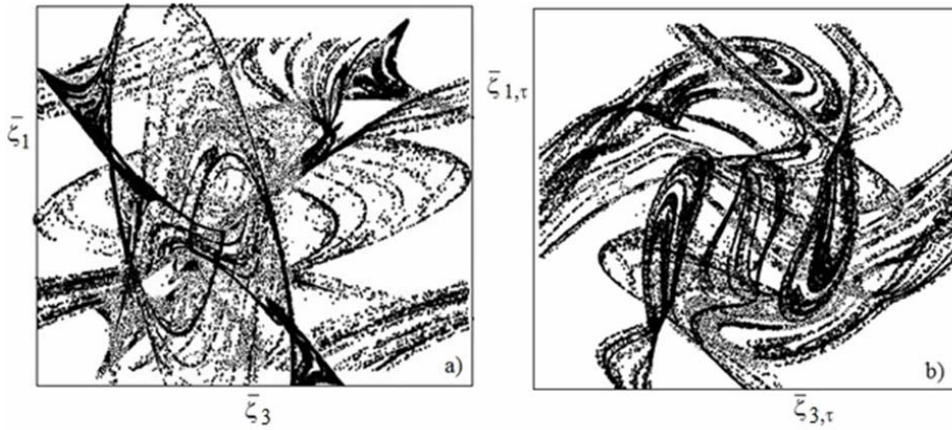


Fig. 10 – The projections of the attractor into planes $(\bar{\zeta}_1, \bar{\zeta}_3)$
and $(\bar{\zeta}_{1,\tau}, \bar{\zeta}_{3,\tau})$ for $a/a_0 = 0.75$.

Five region of stability are depicted in the range of variation $0.5 \leq a/a_0 \leq 1$. The first zone is found to be stable over the range $0.5 \leq a/a_0 < 0.57$. The regions II ($0.57 \leq a/a_0 < 0.69$) and IV ($0.84 \leq a/a_0 \leq 1$) respectively, present instabilities in the motion, while the third region ($0.69 \leq a/a_0 < 0.84$) reports a chaotic behavior. Fig. 11 represents the variation of a/a_0 with respect to time $\tau = t/t_0$, where t_0 is a reference value.

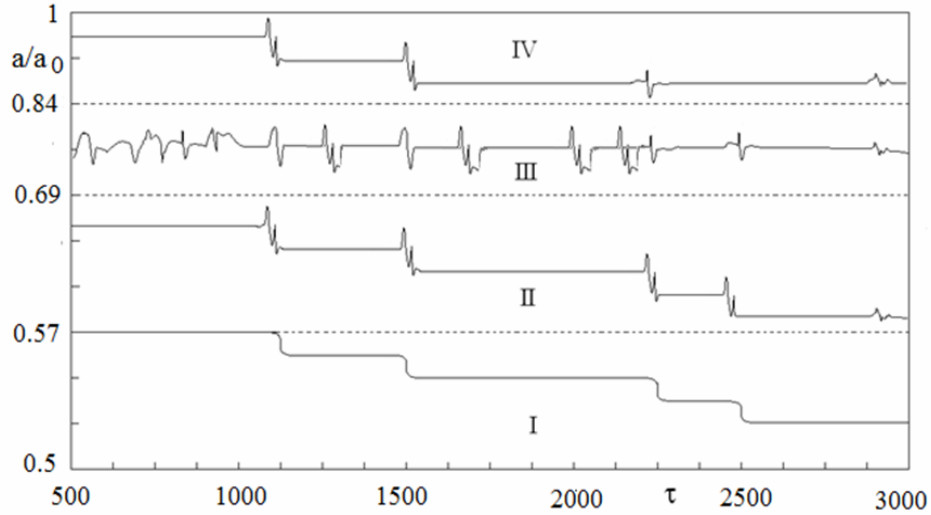


Fig. 11 – Variation of the parameter a/a_0 with respect to time.

The Poincaré cross-section is determined by normal vector $n = (-1.33, 0.69, -2.21, 0.89)$ chosen along the flow solutions $\bar{\zeta}^{(1)}$ and $\bar{\zeta}^{(3)}$ at a base point with coordinates $(0.89, 0.22, 1.76, -0.57)$. Fig. 12a shows the 2D projection of the Poincaré map into the plane $(\bar{\zeta}^{(1)}, \bar{\zeta}^{(3)})$ of the chaotic attractor with two-bundle, for $a/a_0 = 0.8$, and one positive Lyapunov exponent $\lambda_1 = 0.37$.

The chaos-hyperchaos transition occurs when the second Lyapunov exponent becomes positive. By a smooth increasing of $a/a_0 = 0.82$, two Lyapunov exponents $\lambda_1 = 0.39$ and $\lambda_2 = 0.46$ are obtained, and the resulting attractor is a hyperchaotic one, as shown in Fig. 12b. The transition between the chaos and hyperchaos is characterized by an infinite number of unstable periodic orbits which becomes unstable in the least two directions in the vicinity of a transition point. The appearance of the first unstable orbit with more than one unstable direction represents the beginning of the riddling of the basin of attraction and bubbling of the chaotic attractor. This phenomenon is a typical way by which higher-dimensional attractors grow by bursting along the new unstable direction. The orbits $(\bar{\zeta}^{(1)}, \bar{\zeta}^{(3)})$ undergo the instability with respect to both y and z directions, exhibiting the riddling bifurcation.

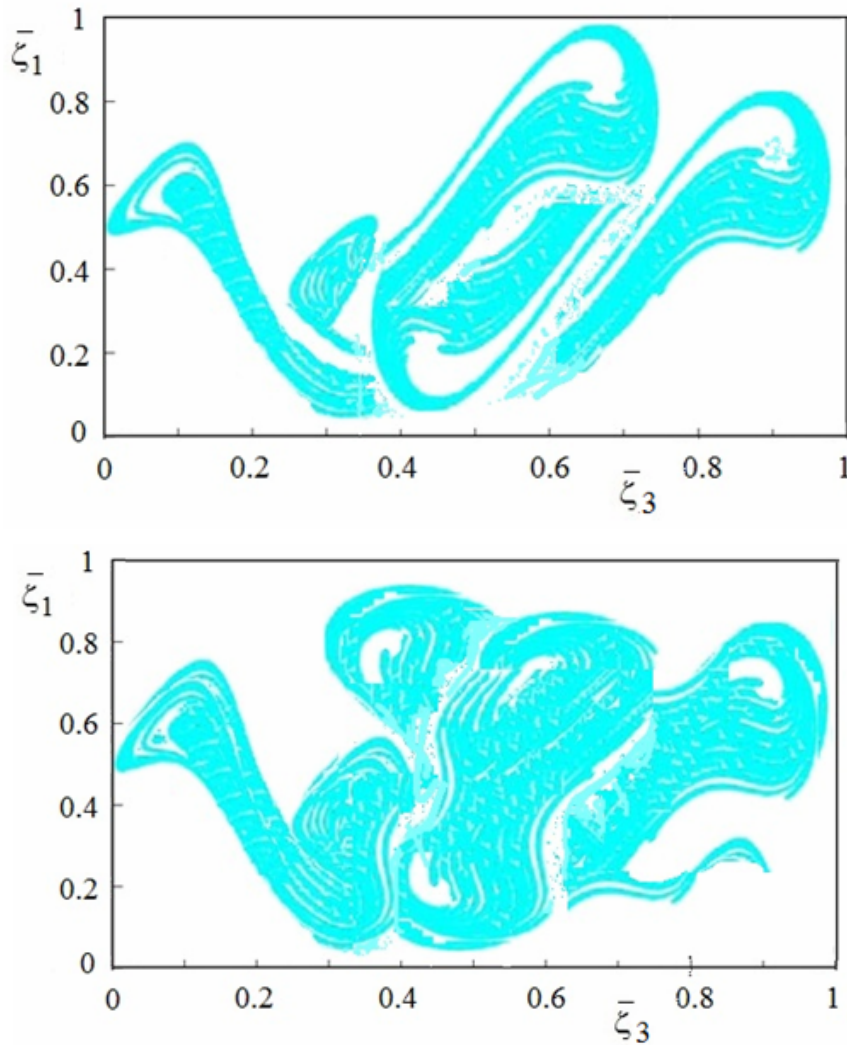


Fig. 12 – 2D projection of the Poincaré map into the plane $(\bar{\zeta}^{(1)}, \bar{\zeta}^{(3)})$ of the attractor: a) chaotic; b) hyperchaotic.

The existence of unstable orbits creates tongues anchored at these orbits, as shown in Fig. 13.

An infinite number of tongues can be created simultaneously, as the result of transverse instability.

The hyperchaotic attractor $(\bar{\zeta}^{(1)}, \bar{\zeta}^{(3)}, \zeta)$ where ζ is the solution of the equation in Z , is displayed in Fig. 14 for $a/a_0 = 0.82$. The initial basin of attraction (green color) is bubbled after the riddling bifurcations.

This means the orbits burst in directions y and z , and in consequence, the chaotic attractor grows. The appearance of the first unstable orbit with more than one unstable direction indicates the activation of growing of the attractor in the higher dimensionality maps.

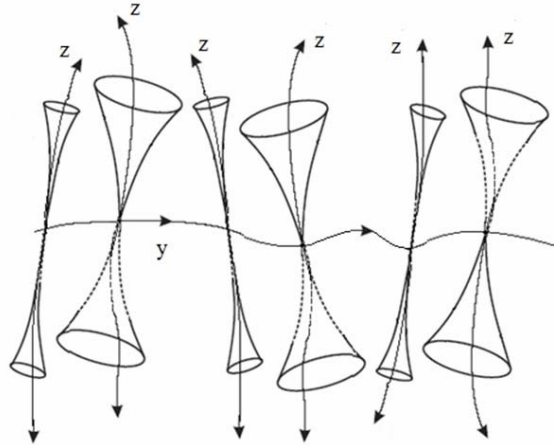


Fig. 13 — Riddling bifurcations of the unstable periodic orbits with respect to y and z .

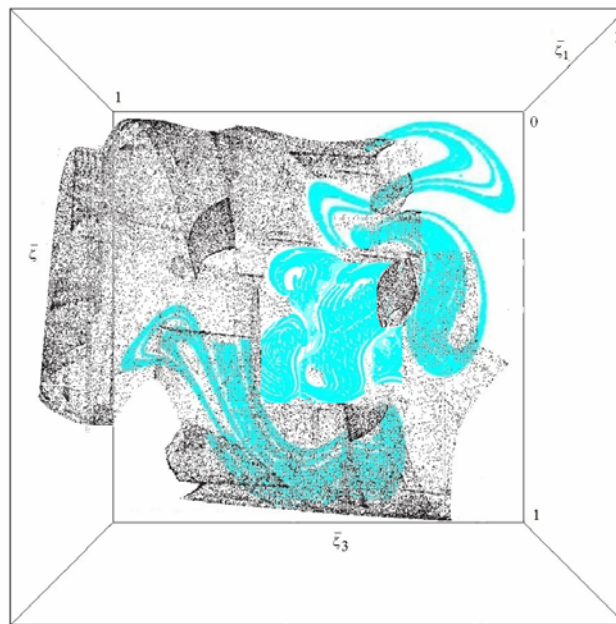


Fig. 14 — The hyperchaotic attractor after riddling bifurcations for $a/a_0 = 0.82$.

5. CONCLUSIONS

The paper discusses a model of baroclinic atmospheric which exhibits the full band-gaps and localised modes around inhomogeneities given by the wind-velocity jumps. The inhomogeneities are modelled as Somigliana dislocations according to the Eshelby theory. The motion of atmosphere tends to chaos when it is subjected to acoustic pulses coming from point source and Gaussian beam of explosive character.

A hyperchaotic attractor with at least two positive Lyapunov exponents is depicted and the presence of disturbances leads to riddling bifurcation that explains the generation of the hyperchaotic attractor. The transition between the chaos and hyperchaos is characterized by an infinite number of unstable periodic orbits which becomes unstable in the least two directions in the vicinity of a transition point.

By initiation of the unstable orbits with more than one unstable direction, the tongues anchored at these orbits undergo the instability with respect to all directions, exhibiting the riddling bifurcations. The main effect of the riddling bifurcation is the bubbling of the attractor, i.e. the orbits burst in all directions and the chaotic attractor grows becoming a hyperchaotic attractor.

Acknowledgements. The authors gratefully acknowledge the financial support of the National Authority for Scientific Research ANCS/UEFISCDI through the project PN-II-ID-PCE-2012-4-0023, Contract no. 3/2013. The authors acknowledge the similar and equal contributions to this article.

Received on May 30, 2016

REFERENCES

1. HIRSEKORN, M., DELSANTO, P.P., BATRA, N.K., MATIC, P., *Modelling and simulation of acoustic wave propagation in locally resonant sonic materials*, Ultrasonics, **42**, 1, pp. 231–235, 2004.
2. GEI, M., *Elastic waves guided by a material interface*, European Journal of Mechanics-A/Solids, **27**, 3, pp. 328–11345, 2008.
3. MIYASHITA, T., *Full band gaps of sonic crystals made of acrylic cylinders in air-numerical and experimental investigations*, Jpn. J. Appl. Phys., **41**, 5S, p. 3170, 2002.
4. MIYASHITA, T., TANIGUCHI, R.; SAKAMOTO, H., *Experimental full band-gap of a sonic-crystal slab structure of a 2D lattice of aluminum rods in air*, Proc. 5th World Congress on Ultrasonics TO-PM04.02, 2003.
5. MUNTEANU, L., CHIROIU, V., *On the dynamics of locally resonant sonic composites*, European Journal of Mechanics-A/Solids, **29**, 5, pp. 871–878, 2010.
6. MUNTEANU, L., BRIŞAN, C., CHIROIU, V., DUMITRIU, D., IOAN, R., *Chaos-hyperchaos transition in a class of models governed by Sommerfeld effect*, Nonlinear Dynamics, **78**, 3, pp. 1877–1889, 2014.

7. MUNTEANU, L., POPESCU, M., *Effects of defects to the band-gaps generation*, PAMM- Proceedings in Applied Mathematics and Mechanics, **14**, 1, pp. 693–694, 2014.
8. JOANNOPOULOS, J.D., JOHNSON, S.D., WINN, J.N., MEADE, R.D., *Photonic Crystals*, Princeton University Press, Second Edition, 2008.
9. NAQUI, J., MARTIN, F., *Some applications of metamaterial resonators based on symmetry properties*, CMC: Computers, materials & Continua, **39**, 3, pp. 267–288, 2014.
10. EADY, E.T., *Long waves and cyclone waves*, Imperial College of Science, London, 1949, pp. 33–52.
11. CHARNEY, J.G., *The dynamics of long waves in a baroclinic westerly current*, Journal of Meteorology, **4**, 5, pp. 136–162, 1947.
12. CHARNAY, B., MEADOWS, V., MISRA, A., LECONTE, L., ARNEY, G., *Modeling of GJ1214b's atmosphere: formation of inhomogeneous high clouds and observational implications*, The Astrophysical Journal Letters, **813**, 1, 2015.
13. CHARNEY, J.G., ELIASSEN, A., *A numerical method for predicting the perturbations of the middle latitude westerlies*, Office of Naval Research of the U. S. Navy, pp. 38–54, 1949.
14. PALMER, T.M., *Edward Norton Lorenz*, Physics Today, **61**, 9, pp. 81–88, 2008.
15. LORENZ, Edward N., *Atmospheric predictability as revealed by naturally occurring analogues*, Journal of the Atmospheric Sciences, **26**, 4, pp. 636–646, 1969.
16. BROJEWSKI, R., *Nonlinear solitary-type structures in the baroclinic model of the atmosphere*, Journal of Technical Physics, **35**, 3, pp. 261–271, 1994.
17. BROJEWSKI, R., JAKUBIAK, B., JASIŃSKI, J., *Dynamics of a 2L-baroclinic model of the troposphere. Part 2: Impact of the zonal drift on bifurcations in the model*, Journal of Technical Physics, **46**, 4, pp. 261–271, 2005.
18. BROJEWSKI, R., JAKUBIAK, B., JASIŃSKI, J., *Impact of the surface temperature and vertical shear of zonal wind on the dynamics of a simple two-layer model of the atmosphere*, Acta Geophysica, **55**, 2, pp. 231–252, 2007.
19. TSUCHIDA, M., GUILHERME, K.L., BALTHAZAR, J.M., *On chaotic vibrations of a non-ideal system with two degree of freedom: 1:2 resonance and Sommerfeld effect*, Journal of Sound and Vibration, **282**, 3, pp. 1201–1207, 2005.
20. ESHELBY, J.D., *The elastic field outside an ellipsoidal inclusion*, Proc. R. Soc. Lond. A, **252**, pp. 561–569, 1959.
21. ESHELBY, J.D., *Elastic inclusions and inhomogeneities*, in: *Progress in solid mechanics*, Vol. 2 (Eds. Sneddon I.N., Hill R.), Amsterdam, The Netherlands: North-Holland, 1961, pp. 89–140.
22. ESHELBY, J.D., *The determination of the elastic field of an ellipsoidal inclusion and related problems*, Proc. R. Soc. Lond. A, **241**, pp. 376–396, 1957.
23. BRIȘAN, C., MUNTEANU, L., CHIROIU, V., ILIE, R., *Scattering of acoustical waves by periodic arrays of scatterers*, Acta Technica Napocensis, Series: Applied Mathematics and Mechanics, **56**, 4, pp. 625–630, 2013.
24. XU, G., YAN, S., MA, Q.W., *Modified SFDI for fully nonlinear wave simulations*, CMES: Computer Modeling in Engineering & Sciences, **106**, 1, pp. 1–35, 2015.
25. ROSSLER, O.E., *An equation for continuous chaos*, Physics Letters A, **57**, 5, pp. 397–398, 1976.
26. WARMINSKI, J., BALTHAZAR, J.M., BRASIL, R.M.L.R.F., *Vibrations of a non-ideal parametrically and self-excited model*, Journal of Sound and Vibration, **245**, 2, pp. 363–374, 2001.
27. VALLEJO, J.C., SANJUAN, M.A.F., *Predictability of orbits in coupled systems through finite-time Lyapunov exponents*, New Journal of Physics, **15**, 11, p. 113064, 2013.
28. KAPITANIAK, T., *Chaos synchronization and hyperchaos*, Journal of Physics: Conference Series, **23**, pp. 317–324 International Conference on Control and Synchronization of Dynamical Systems, 2005.
29. KAPITANIAK, T., CHUA, L.O., ZHONG, Q.G., *Experiment hyperchaos in coupled Chua's circuits*, IEEE Transactions on Circuits and Systems, **41**, 7, pp. 499–503, 1994.

30. PEINKE, M.J., PARISI, J., ROSSLER, O.E., STOOP, R., *Encounter with chaos*, Springer: Berlin, 1992.
31. MUNTEANU, L., CHIROIU, V., SIRETEANU, T., *On the response of small buildings to vibrations*, *Nonlinear Dynamics*, **73**, 3, pp. 1527–1543, 2013.
32. MUNTEANU, L., CHIROIU, V., DONESCU, St., BRIȘAN, C., *A new class of sonic composites*, *Journal of Applied Physics*, **115**, 10, p. 104904, 2014.
33. FELIX, J.L.P., BALTHAZAR, J.M., *Comments on a nonlinear and nonideal electromechanical damping vibration absorber, Sommerfeld effect and energy transfer*, *Nonlinear Dynamics*, **55**, 1, pp. 1–11, 2009.
34. GIRIP, I., IOAN, R., *On the contact interfaces in the sonic composites*, *PAMM - Proceedings in Applied Mathematics and Mechanics*, **14**, 1, pp. 357–358, December 2014.
35. ILIE, R., IOAN, R., BRIȘAN, C., *On the sonic composites subjected to severe acoustic loads*, *PAMM- Proceedings in Applied Mathematics and Mechanics*, **14**, 1, pp. 687–688, 2014.
36. CHIROIU, V., MUNTEANU, L., DUMITRIU, D., RUGINA, C., BRISAN, C., *Anti-sound and acoustical cloaks*, *Scientific Bulletin of The “Petru Maior” University of Târgu-Mureș*, **13**, 2, pp. 5–11, 2016.
37. MUNTEANU, L., DONESCU, St., *Introduction to Soliton Theory: Applications to Mechanics*, *Book Series Fundamental Theories of Physics*, Vol. 143, Kluwer Academic Publishers, Dordrecht, Boston (Springer, Netherlands), 2004.